PHYSICAL REVIEW B **103**, 085110 (2021)

Oxygen vacancy induced site-selective Mott transition in $LaNiO_3$

Xingyu Liao,[1] Vijay Singh,[1] and Hyowon Park[1,2]
[1]*Department of Physics, University of Illinois at Chicago, Chicago, Illinois 60607, USA*
[2]*Materials Science Division, Argonne National Laboratory, Argonne, Illinois 60439, USA*

(Received 10 November 2020; accepted 25 January 2021; published 8 February 2021)

While defects such as oxygen vacancies in correlated materials can modify their electronic properties dramatically, understanding the microscopic origin of electronic correlations in materials with defects has been elusive. Lanthanum nickelate with oxygen vacancies, $LaNiO_{3-x}$, exhibits the metal-to-insulator transition as the oxygen vacancy level x increases from the stoichiometric $LaNiO_3$. In particular, $LaNiO_{2.5}$ exhibits a paramagnetic insulating phase, also stabilizing an antiferromagnetic state below $T_N \simeq 152$ K. Here, we study the electronic structure and energetics of $LaNiO_{3-x}$ using first principles. We find that $LaNiO_{2.5}$ exhibits a "site-selective" paramagnetic Mott insulating state at $T \simeq 290$ K as obtained using density functional theory plus dynamical mean field theory (DFT + DMFT). The Ni octahedron site develops a Mott insulating state with strong correlations as the Ni e_g orbital is half-filled while the Ni square-planar site with apical oxygen vacancies becomes a band insulator. Our oxygen vacancy results cannot be explained by the pure change of the Ni oxidation state alone within the rigid band-shift approximation. Our DFT + DMFT density of states explains that the peak splitting of unoccupied states in $LaNiO_{3-x}$ measured by the experimental x-ray absorption spectra originates from two nonequivalent Ni ions in the vacancy-ordered structure.

DOI: 10.1103/PhysRevB.103.085110

I. INTRODUCTION

Rare-earth nickelates $R\text{NiO}_3$ (R is the rare-earth ion) have attracted significant research interests due to their rich electronic properties. These include the metal-insulator transition, charge order, magnetism, multiferroicity, and the site-selective Mott transition [1–6]. Although the R ion can be treated as electrically inert, the phase boundaries of the metal-to-insulator transition and the paramagnetic (PM) to antiferromagnetic (AFM) transition depend sensitively on the subtle structural tolerance factor controlled by the size of the R ion [7]. This close interplay between the structural, electronic, and magnetic degrees of freedom puts the rare-earth nickelate into an intriguing correlated material.

Oxygen vacancy is one of the common defects in transition metal oxides and it can play a central role in oxide electronics [8]. It is also known that oxygen vacancies in $LaNiO_3$, one of the rare-earth nickelates, also change their electronic and magnetic properties significantly as they can modify electronic correlation effects. Although $LaNiO_3$ is the only metallic case among the known rare-earth nickelate series, Ni d orbitals are still moderately correlated as indicated by experimental spectroscopic measurements [9–11]. Experimental measurements on the conductivity in $LaNiO_{3-x}$ show that the increase of the vacancy level x reduces the conductivity and the metal-to-insulator transition occurs as x approaches to 0.5 [12,13]. As the oxygen vacancy level x increases further, $LaNiO_{2+\delta}$ is found to be semiconducting or poorly conducting [14]. The complete absence of the apical oxygens leads to the infinite-layer structure of $LaNiO_2$ and the role of electronic correlations in $LaNiO_2$ has been drawing much attention recently as similar nickelates such as $NdNiO_2$ and $PrNiO_2$ exhibit superconductivity when they are hole doped [15,16]. Although $LaNiO_2$ is metallic, resistivity increases at low temperatures, hinting possibly strong correlation effects.

In addition to transport properties, oxygen vacancies also have significant effects on magnetism. Although $LaNiO_3$ has been known to remain PM at all temperatures, there was a controversial experimental work showing some evidence of AFM orders in $LaNiO_3$ [17]. It was also argued that AFM in $LaNiO_3$ can be originated from small oxygen vacancies [18,19]. As oxygen vacancy level further increases, $LaNiO_{2.5}$ becomes AFM below 152 K, and $LaNiO_{2.75}$ shows ferromagnetic (FM) structure below 225 K [19]. However, $LaNiO_2$ does not show any clear evidence of the long-range magnetic order [20].

Spectroscopic measurements of $LaNiO_{3-x}$ are also widely performed using x-ray absorption spectroscopy (XAS) and photoemission spectroscopy (PES) to study electronic structure in experiments. Consistently with the transport measurement, spectra at the Fermi energy decrease as the vacancy level x increases from $LaNiO_3$, opening a spectral gap near the level at $x = 0.5$. An interesting feature measured from XAS in $LaNiO_{3-x}$ bulk [21,22] as well as the thin-layer structure [23] is the splitting of the spectral peak above the Fermi energy, which has been attributed to the oxygen vacancy effect.

There have been some first-principles studies of magnetism and oxygen vacancy effects on rare-earth nickelates. Previous density functional theory (DFT) and *GW* study on $LaNiO_{3-x}$ systems addressed the metal-insulator transition and resulting spectra due to the vacancy effect [24]. Malashevich *et al.* [25] did a systematic study on $LaNiO_{3-x}$ with small x value and found that oxygen vacancies stay around the same Ni ion and localize extra electrons created by the vacancy. The strong localization of electrons due to the oxygen vacancies in other rare-earth nickelates also has been studied using DFT + U [26]. Subedi *et al.* [27] studied structural and magnetic instabilities in $LaNiO_3$ with possible breathing-type lattice distortions using DFT and DFT + U. Theoretical studies on RNiO$_2$ with $R =$ La, Nd, Sr, and Pr have attracted much attention recently as they can serve as model systems of experimentally discovered nickelate superconductors [28–34]. Nevertheless, the microscopic origin of the strongly correlated insulating phase induced by oxygen vacancies and the changes of the correlated spectra in $LaNiO_{3-x}$ compared to experiments have not been systematically investigated.

In this paper, we study the strong correlation effect on the electronic structure and the energetics of $LaNiO_{3-x}$ from first principles as the oxygen vacancy level x evolves. We adopt dynamical mean field theory (DMFT) in combination with DFT to treat strong correlations in the paramagnetic phase as well as DFT + U for the long-range magnetic state. We show that the vacancy-ordered structure becomes thermodynamically stable in $LaNiO_{2.5}$ and the metal-to-insulator transition due to the change of the vacancy level x can be captured correctly in DFT + DMFT. The insulating nature of the vacancy-ordered $LaNiO_{2.5}$ structure with two nonequivalent Ni ions originates from the site-selective Mott phase due to both structural and electronic correlation effects. While bulk $LaNiO_3$ forms a rhombohedral structure with the octahedral geometry of the Ni ion surrounded by six O ions, oxygen vacancies can change both the oxidation number of the Ni ion and the local structure, which can lead to the substantial change of electronic structures in $LaNiO_{3-x}$.

Our paper is organized as follows. First, we explain the computational methods we used including DFT, DFT + U, and DFT + DMFT in Sec. II and show the structural details and magnetism in Sec. III A. We also study formation energies of $LaNiO_{3-x}$ in Sec. III B. Then, we display the spectral functions of $LaNiO_{3-x}$ computed using DFT + DMFT and DFT + U, and compare to experimental measurements in Sec. III C. The DMFT self-energies in $LaNiO_{3-x}$ are displayed to explain the nature of the insulating phase in Sec. III D and compare our results to the rigid band-shift approximation in Sec. III E. We conclude our discussion in Sec. IV.

II. COMPUTATIONAL METHODS

First, we performed structural relaxation calculations for $LaNiO_{3-x}$ ($x = 0, 0.25, 0.5, 0.75$, and 1) systems and obtained the ground-state energies and magnetism using both DFT and DFT + U. Vienna *ab initio* simulation package (VASP) [35,36] has been used in all DFT and DFT + U calculations adopting the Perdew-Burke-Ernzerhof for solids (PBE-sol) [37] as the exchange and correlation energy functional. We set 600 eV as the energy cutoff for the plane-wave basis and a Gaussian smearing of 0.2 eV is used for the summation over the Monkhorst-Pack k-point mesh. For $LaNiO_3$, $LaNiO_{2.5}$, and $LaNiO_2$ structures, we use a $8 \times 8 \times 8$ k-point grid. $LaNiO_{2.25}$ and $LaNiO_{2.75}$ have a rather large supercell with a long lattice vector along the y direction, therefore, we use a $6 \times 3 \times 6$ k grid. For all structural relaxations, we set 0.001 eV/Å as the force convergence condition fully relaxing the cell shape, volume, and internal ionic positions.

Then, we calculate the correlated electronic structure using DFT + DMFT and DFT + U for $LaNiO_3$, $LaNiO_{2.5}$, and $LaNiO_2$. While DFT + U can capture static correlations beyond DFT at the Hartree-Fock level based on single-determinant wave functions, DFT + DMFT can go beyond the static approximation in DFT + U and capture dynamical correlations based on multideterminant many-body wave functions. To study magnetism, DFT + U is adopted to relax structures imposing experimental magnetic orderings and to study the electronic structure from those relaxed structures. For a paramagnetic state, we adopt DFT + DMFT using the DFT relaxed structure with the nonmagnetic (NM) order. The relaxed structures obtained using DFT and DFT + U are quite similar, as will be shown in the next section. We adopt the DMFTwDFT package [38] for DFT + DMFT calculations. The WANNIER90 package [39,40] has been adopted to obtain maximally localized Wannier functions for the construction of the DMFT correlated subspace. Nickelates show a rather strong d-p hybridization due to the covalent bonding between Ni and O ions. Therefore, it is important to construct both Ni 3d and O 2p orbitals for the Wannier basis to treat the hybridization effect. To construct the Wannier orbitals, we take an energy window from −9 to 5 eV from the Fermi energy, which are basically all Ni 3d and O 2p orbitals.

For DFT + U and DFT + DMFT, we need to define interaction parameters to treat the onsite Coulomb interaction within the d orbitals of the Ni ion. A rather small value of $U(\simeq 2$ eV) was used in the d-orbital model of previous rare-earth nickelates studies [41,42] while $U = 5 \sim 7$ eV was used for the wide-energy window calculation including both d and p orbitals to reproduce the metal-insulator and structural phase diagram and to compare with the angle-resolved photoemission spectra [43,44]. Similar U value ($\simeq 5.7$ eV) was also obtained from the constrained DFT calculation using the QUANTUM ESPRESSO code [45]. For both DFT + DMFT and DFT + U calculations in this paper, we use the Hubbard $U = 5$ eV and the Hund's coupling $J = 0.8$ eV which are parametrized by the Slater integrals. To account for the double-counting correction of DFT + DMFT, the modified fully-localized-limit form of the double-counting potential, which was used for the phase diagram study of rare-earth nickelates [43,46], has been used. To solve the DMFT impurity problem, we use the continuous-time quantum Monte Carlo [47,48] solver with temperature $T \approx 290$ K. After DFT + DMFT calculations are converged, we used the post-processing tool from the DMFTwDFT package to calculate the spectral function A(ω) for $LaNiO_{3-x}$. More details of the DMFT calculation method are shown in the Supplemental Material [49].

III. RESULTS

A. Structural relaxation and magnetism

Bulk $LaNiO_3$ forms a rhombohedral structure given by the $R\bar{3}c$ space symmetry group [50]. This structure has two La, two Ni, and six O ions in a unit cell, which can be obtained by rotating the Ni-O octahedra from the cubic perovskite

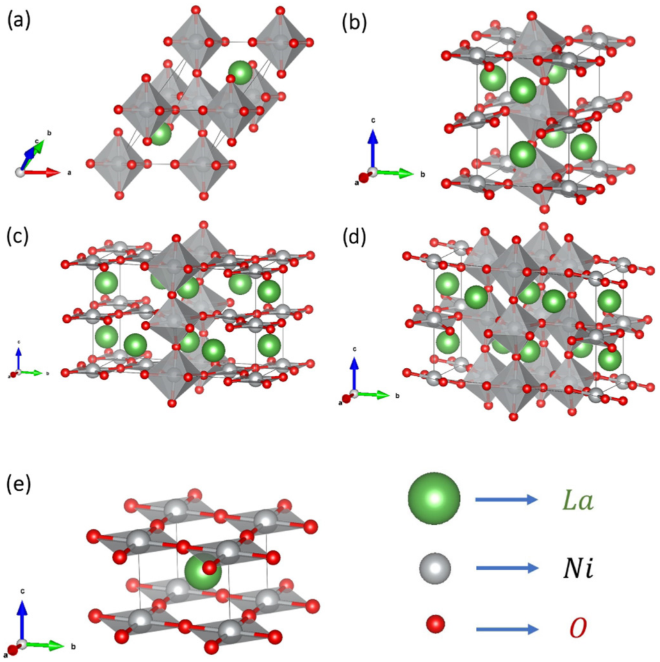

FIG. 1. Crystal structures of (a) $LaNiO_3$, (b) $LaNiO_{2.5}$, (c) $LaNiO_{2.25}$, (d) $LaNiO_{2.75}$, and (e) $LaNiO_2$

structure. Namely, without any defects, each Ni ion is surrounded by six O ions forming the octahedron and all Ni-O octahedra are equivalent with the same Ni-O bond lengths [see Fig. 1(a)]. The oxygen vacancy formation induces the local structural distortion due to the absence of apical oxygens, which breaks the cubic symmetry. While it is challenging to measure the crystal structure with vacancies, several experiments [13,51,52] suggest the $LaNiO_{2.5}$ structure such that NiO_6 octahedra and NiO_4 square planes are alternating in the x-y plane as shown in Fig. 1(b). Previous DFT calculation [25] also provides the insight that the apical divacancy configuration lowers the formation energy than other configurations meaning a four-coordinated Ni-O square plane is energetically favored when oxygen vacancies are introduced. In this paper, we denote Ni in the octahedral environment as Ni_o and Ni in the square-planar symmetry as Ni_{sp}. We also construct $LaNiO_{2.25}$ and $LaNiO_{2.75}$ structures with vacancy orderings such that Ni_o and Ni_{sp} ions modulated along the x-y plane, as shown in Figs. 1(c) and 1(d). $LaNiO_2$ becomes a tetragonal structure of purely Ni_{sp} ions with NiO_4 square planes [see Fig. 1(e)].

While $LaNiO_3$ remains a PM metallic state at all temperatures, $LaNiO_{3-x}$ ($x > 0$) undergoes the magnetic transition for most cases. In Table I, we list the experimentally observed long-range magnetic orderings of $LaNiO_{3-x}$ including the ground state (metal or insulator) and the Neel temperature (T_N) with relevant references. Most $LaNiO_3$ structures with O vacancies become FM except $LaNiO_{2.5}$. Previous experimental work [51] in $LaNiO_{2.5}$ suggests that $LaNiO_{2.5}$ is the G-type AFM and the Ni_o ions have relatively large magnetic moments, while the Ni_{sp} ions have almost no magnetic moment. All $LaNiO_{3-x}$ structures become paramagnetic above T_N.

TABLE I. Experimental magnetic and transport (metal/insulator) properties of $LaNiO_{3-x}$.

$LaNiO_{3-x}$	M/I	Mag.	T_N
$LaNiO_3$ [13,18]	M	PM	0 K
$LaNiO_{2.75}$ [13,19]	M	FM	225 K
$LaNiO_{2.53}$ [52]		FM	
$LaNiO_{2.5}$ [13,19]	I	AFM	152 K
$LaNiO_2$ [14,20]	M	PM	

To study the structural and magnetic properties, we fully relaxed the oxygen vacancy-ordered structures of $LaNiO_{3-x}$ with $x = 0$, 0.25, 0.5, 0.75, and 1 using both DFT and DFT + U. In Table II, we provide the structure details obtained from the relaxations with magnetic structures observed in experiments for $x = 0$, 0.5, and 1. That is to say, we impose the G-type AFM order on $LaNiO_{2.5}$ relaxations. The nonmagnetic (NM) order calculations on $LaNiO_2$ and $LaNiO_3$ are performed to simulate PM nature in experiment. In $LaNiO_3$, DFT Ni-O bond length and Ni-O-Ni bond angle are similar to experiment while DFT + U overestimate the bond angle along with the contracted bond length. $LaNiO_{2.5}$ has two nonequivalent Ni ions and the Ni_o-O bond length is much larger than the Ni_{sp}-O bond length. $LaNiO_{2.5}$ structure relaxed with DFT shows the Ni-O bond length difference to be 0.14 Å. DFT + U predicts the similar Ni-O bond difference (∼0.22 Å) as the experimental value (∼0.21 Å) although the absolute values of the bond lengths in DFT + U are smaller than experimental values. In $LaNiO_2$, the Ni-Ni distance along the z axis is quite smaller than along the x-y plane due to the loss of apical oxygens and the DFT structural parameters are closer to experimental values than the DFT + U parameters.

In Table III, we calculate the ground-state energies of $LaNiO_{3-x}$ using DFT and DFT + U. Different magnetic orderings including G-type AFM, FM, and NM order are imposed during the relaxation calculations and subtract the resulting FM energy from the G-type AFM energy for each system. In each structure, different magnetism can be obtained by converging the solutions from different initial configurations. In $LaNiO_3$, the ground state converges to the NM

TABLE II. Structural information of $LaNiO_3$, $LaNiO_{2.5}$, and $LaNiO_2$ obtained from DFT and DFT + U relaxations.

	Parameters	DFT	DFT + U	Expt.
$LaNiO_3$	$d_{\text{Ni-O}}$ (Å)	1.90	1.88	1.93 [53]
(NM)	$\alpha_{\text{Ni-O-Ni}}$ (deg)	164.5	168.3	164.8 [53]
$LaNiO_{2.5}$	$d_{\text{Ni-Ni}}{}^{a}$ (Å)	3.83	3.82	3.91 [51]
(AFM)	$d_{\text{Ni-Ni}}{}^{b}$ (Å)	3.64	3.67	3.74 [51]
	$d_{\text{Ni}_{sp}\text{-O}}$ (Å)	1.86	1.83	1.91 [51]
	$d_{\text{Ni}_{o}\text{-O}}{}^{a}$ (Å)	2.00	2.05	2.12 [51]
	$d_{\text{Ni}_{o}\text{-O}}{}^{b}$ (Å)	1.86	1.88	1.92 [51]
$LaNiO_2$	$d_{\text{Ni-Ni}}{}^{a}$ (Å)	3.89	3.84	3.96 [20]
(NM)	$d_{\text{Ni-Ni}}{}^{b}$ (Å)	3.34	3.32	3.37 [20]
	$d_{\text{Ni-O}}{}^{a}$ (Å)	1.95	1.92	1.98 [20]

[a] Along the x-y plane.
[b] Along the z axis.

TABLE III. Total energy difference per formula unit (meV) between FM and AFM in $LaNiO_{3-x}$.

$LaNiO_{3-x}$	DFT AFM-FM	DFT + U AFM-FM
$LaNiO_3$	0[a]	341
$LaNiO_{2.75}$	4	40
$LaNiO_{2.5}$	10	−41
$LaNiO_{2.25}$	2	68
$LaNiO_2$	20[b]	−51

[a] Both FM and AFM converged to zero magnetic moment.

[b] FM converged to zero magnetic moment.

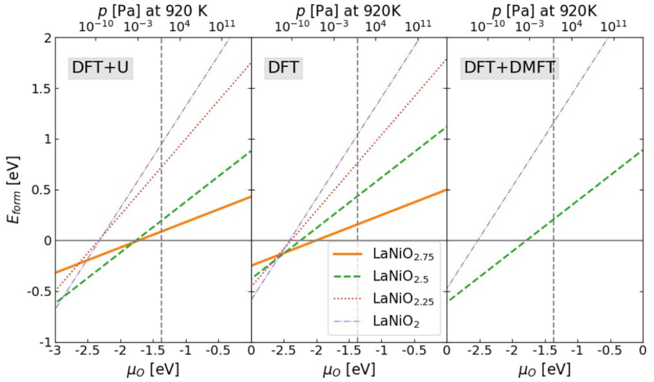

FIG. 2. Formation energies E_{form} of $LaNiO_{3-x}$ as a function of the oxygen chemical potential μ_O (related to the oxygen pressure P) calculated using DFT + U (at $T = 0$ K), DFT (at $T = 0$ K), and DFT + DMFT (at $T = 920$ K). The vertical dashed line indicates the typical oxygen pressure used in experiment.

structure regardless of FM or AFM initial configurations in DFT while DFT + U predicts it to be FM. Also in $LaNiO_2$, DFT converges to the NM configuration while AFM is more stable in DFT + U. In $LaNiO_{2.5}$, DFT + U predicts the ground state to be AFM consistently with the experiment (see Table I) while DFT converges to the FM ground state. This implies that the correlation treated in DFT + U can be important to capture the ground-state magnetic configuration in structures with vacancies. Both DFT and DFT + U give the FM order lower energy than AFM order in $LaNiO_{2.75}$, which is also consistent with experiments.

In $LaNiO_{2.5}$, the spin-state ordering occurs as the Ni_o ion in NiO_6 exhibits a high-spin state while the Ni_{sp} ion in NiO_4 shows a low-spin state [51]. This spin-state ordering induced by the oxygen vacancy ordering is also consistent with our DFT + U calculation. We find the Ni_o ion shows a high-spin state with the magnetic moment of $1.62\mu_B$, which is much larger than the low-spin moment in Ni_{sp} ($0.16\mu_B$). This spin-state ordering is also accompanied by the in-plane Ni-O bonding disproportionation in which the Ni_o-O bond length is much larger than the Ni_{sp}-O bond length by ∼0.22 Å (see Table II). $LaNiO_{2.75}$ and $LaNiO_{2.25}$ with FM order also show the similar trends of the spin-state ordering in our calculations in that the Ni_o ion has a larger moment than the Ni_{sp} ion, as shown in Table IV.

B. Formation energies

The stability of the oxygen vacancy-ordered structure can be determined by the formation energy calculation. Here, we compute the vacancy formation energy per formula unit for $LaNiO_{3-x}$ structures as a function of the oxygen chemical potential related to the given oxygen pressure. The formation energy can be given by [54]

$$E_{\text{form}} = E_{LaNiO_{3-x}} - E_{LaNiO_3} + x\tfrac{1}{2}E_{O_2} + x\mu_O, \qquad (1)$$

where E_{form} is the Gibbs formation energy, x is the vacancy level, $E_{LaNiO_{3-x}}$ is the total energy of $LaNiO_{3-x}$, E_{O_2} is the total energy of the O_2 molecule, and μ_O is the oxygen chemical potential depending on pressure and temperature. Here, we neglect the phonon and entropy contributions of $LaNiO_{3-x}$ to the Gibbs formation energy at finite temperatures. In experiments, the thermodynamic stability condition of oxygen vacancies in given materials can depend on the applied oxygen pressure P and temperature T. We assume that the oxygen molecule forms an ideal-gas-like reservoir during the experimental sample growth, therefore, its chemical potential can be given by [54–57]

$$\mu_O(T, P) = \mu_O(T, P^0) + \frac{1}{2}k_BT\ \ln\left(\frac{P}{P^0}\right), \qquad (2)$$

where P^0 is the ambient pressure. The $\mu_O(T, P^0)$ values are taken from Ref. [55]. Typical experimental growth of $LaNiO_3$ on the $SrTiO_3$ substrate is carried out at around 920 K and 10 Pa oxygen pressure [22].

TABLE IV. Magnetic moments (μB) of $LaNiO_{3-x}$ computed using DFT + U.

$LaNiO_{3-x}$	Ni_o	Ni_{sp}
$LaNiO_{2.75}$ (FM)	1.04/1.47/1.04	0.11
$LaNiO_{2.5}$ (AFM)	1.62	0.16
$LaNiO_{2.25}$ (FM)	1.60	0.8/0.8/0.8

In Fig. 2 we plot E_{form} as a function of μ_O (related to the applied pressure) at 920 K computed using DFT + U, DFT, and DFT + DMFT. We compute the total energies of $LaNiO_{3-x}$ in Eq. (1) using first-principles (DFT, DFT + U, and DFT + DMFT) by adopting the same relaxed structures of $LaNiO_{3-x}$ as used in the spectra calculations. We choose the magnetic order in DFT or DFT + U calculations resulting the lowest energy while DFT + DMFT calculations adopt the PM order for all $LaNiO_{3-x}$ structures at 920 K. Our results suggest that, for the oxygen-rich region, when the oxygen pressure higher than 55 Pa (corresponding to $\mu_o > -1.3$ eV), $LaNiO_3$ is the most stable structure compared to other vacancy structures with the positive vacancy formation energies. However, as the oxygen pressure is lowered than 4.5 Pa (corresponding to -2.1 eV $< \mu_o < -1.4$ eV), we find that $LaNiO_{2.5}$ becomes the most stable structure in the DFT + U calculation although different vacancy structures have very similar formation energies in DFT. DFT + DMFT also shows the similar energetics as a function of the oxygen pressure compared to DFT + U implying that correlation effects in DFT + DMFT or DFT + U treated beyond DFT can be important to capture

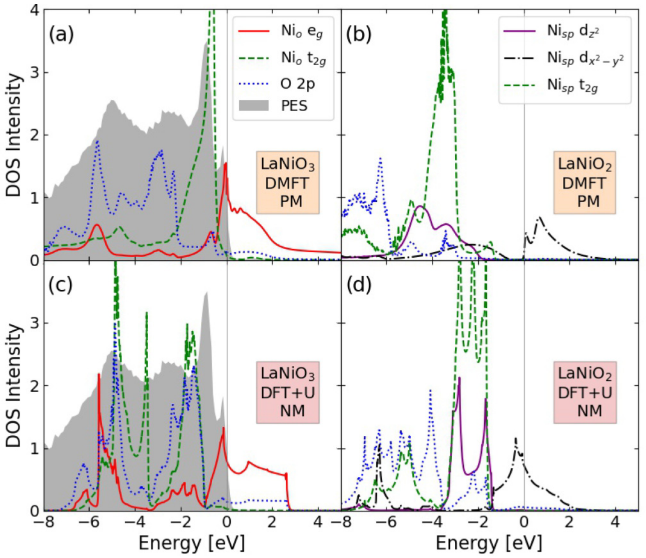

FIG. 3. The orbital-resolved DOS of $LaNiO_3$ (a), (c) and $LaNiO_2$ (b), (d) computed using DFT + DMFT (a), (b) and DFT + U (c), (d). The e_g orbitals in $LaNiO_3$ are degenerate. The shaded region is taken from the experimental PES measurement [22].

the correct formation energy in oxygen vacancy structures. Since DFT + U (DFT + DMFT) can capture the correct AFM (PM) order as well as the insulating state in $LaNiO_{2.5}$, the predicted vacancy-ordered structure from first principles can be indeed stable under the experimental growth condition of the lower oxygen pressure region.

C. Correlated density of states

In this section, we study the correlated density of states (DOS) for the vacancy-ordered structure in $LaNiO_{2.5}$ as well as stoichiometric $LaNiO_3$ and $LaNiO_2$ using both DFT + DMFT and DFT + U to treat correlations beyond DFT. First, we compare the DOS for stoichiometric $LaNiO_3$ [$x = 0$; Fig. 3(a)] and $LaNiO_2$ [$x = 1$; Fig. 3(b)] computed using DFT + DMFT. $LaNiO_3$ computed using DFT + DMFT shows the Fermi-liquid metal feature, which is consistent with the experimental measurement [9]. The overall peak positions computed in DFT + DMFT are also consistent with the experimental PES peak positions [22]. Our orbital-resolved DFT + DMFT DOS reveals that the small bump below the Fermi energy has mostly the Ni e_g character and the sharp peak near −0.7 eV is mostly contributed from the t_{2g} character although O 2p orbitals are also mixed with these orbitals. O 2p peaks are distributed broadly below −2 eV. The unoccupied DOS also shows a broad e_g peak with a strong mixture with O 2p spectra due to the covalent bonding between Ni and O ions. As a result, the hole density per the O ion is 0.26 and the occupancy of the Ni 3d orbital becomes ~7.8 (see Table V).

The absence of apical oxygens in $LaNiO_2$ changes electronic structures significantly compared to $LaNiO_3$. First, the apical oxygen vacancy breaks the symmetry of the Ni-O octahedron and splits the onsite orbital energies within e_g and t_{2g} manifolds as the local geometry of the Ni-O bonding becomes a square-planar symmetry. As a result, two e_g orbitals in Ni_{sp} become nondegenerate and the d_{z^2} orbital is lower in energy than the $d_{x^2-y^2}$ orbital. Second, the removal of the apical oxygen ions from the Ni-O octahedron means that two electrons are effectively donated to the remaining Ni-O square plane. The donation of two electrons from the apical oxygen changes the oxidation state of Ni^{3+} in $LaNiO_3$ to Ni^{1+} in $LaNiO_2$. Due to this electron transfer, d occupancy in Ni_{sp} becomes close to 9.1 while the hole per O ion is also reduced to 0.06 (see Table V). As a result, the d_{z^2} orbital tends to be fully filled while the $d_{x^2-y^2}$ orbital is almost half-filled, enhancing the electronic correlation effect.

TABLE V. Occupations of Ni 3d and O 2p orbitals in $LaNiO_{3-x}$ obtained from DFT+DMFT and DFT + U.

DFT+DMFT	Ni_o	Ni_{sp}	O_{avg}
$LaNiO_3$ (PM)	7.79		5.74
$LaNiO_{2.5}$ (PM)	8.15	8.57	5.86
$LaNiO_2$ (PM)		9.12	5.94
DFT + U			
$LaNiO_3$ (NM)	8.23		5.59
$LaNiO_{2.5}$ (AFM)	8.27	8.73	5.80
$LaNiO_2$ (NM)		9.30	5.85

Our DMFT DOS in $LaNiO_2$ is also consistent with the experimental XAS measurement [58] showing the strong reduction of the unoccupied O 2p spectra compared to the $LaNiO_3$ case. Our unoccupied O 2p DOS [blue dashed line in Fig. 3(b)] is also much reduced and the occupied O 2p peak in $LaNiO_2$ is located further below the Fermi energy due to the reduced hole density in the O ion and the decreased Ni-O hybridization compared to $LaNiO_3$. Due to this much reduced Ni-O hybridization and the $d_{x^2-y^2}$ orbital occupancy close to the half-filling, the $LaNiO_2$ becomes close to the Mott insulating phase as reflected in the strong reduction of the $d_{x^2-y^2}$ spectra near the Fermi energy which is also consistent with the experimental XAS measurement [58]. This incoherent metallic state due to the strong correlation effect is also reflected in the large scattering rate [the imaginary part of the self-energy at the zero frequency in Fig. 5(b)] and consistent with the poor conductivity measured experimentally in $LaNiO_2$ [14]. Our DFT band-structure calculation reveals that some La 5d bands are also crossing below the Fermi energy (see Supplemental Material [49]) although we do not include this hybridization effect of the La 5d orbital as we construct the Wannier functions for only Ni 3d and O 2p orbitals. Although treating the effect of this La 5d orbital on the DMFT correlation is beyond the scope of our paper, previous DMFT calculation in the similar $NdNiO_2$ material argues that the Nd 5d band acts as a charge reservoir without significant hybridization with the Ni 3d orbital [30].

In Figs. 3(c) and 3(d), we also plot the orbital-resolved DOS for both $LaNiO_3$ and $LaNiO_2$ obtained using DFT + U. We impose the NM spin order for both materials, consistently with the experiment as listed in Table I. In both materials, the DFT + U calculations also exhibit qualitatively similar features as the DFT + DMFT spectra. In $LaNiO_3$, the t_{2g} peak is located slightly below the experimental peak at −0.7 eV and it is somewhat strongly hybridized with O p orbitals. Consistently with DMFT, the unoccupied O 2p DOS becomes much

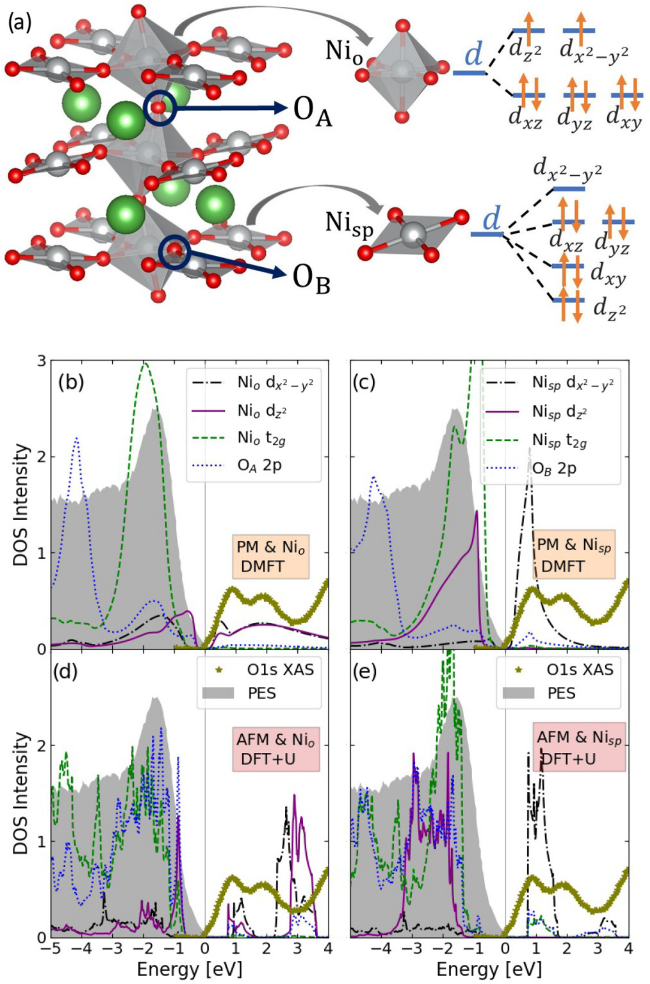

FIG. 4. (a) The crystal structure of NiO$_{2.5}$ showing two nonequivalent Ni ions with the distinct orbital energy level diagram. The site- and orbital-resolved DOS of LaNiO$_{2.5}$ obtained using DFT + DMFT (b), (c) and DFT + U (d), (e) computed for Ni$_o$ (b), (d) and Ni$_{sp}$ (c), (e). PES and XAS data are taken from experimental measurements [22].

reduced in LaNiO$_2$ and $d_{x^2-y^2}$ orbital is also nearly half-filled. However, the DFT + U spectra have still large DOS intensity at Fermi level and the O 2p peak is relatively close to the Fermi energy compared to DMFT.

Now, we turn to the LaNiO$_{2.5}$ case with the oxygen vacancy ordering. We performed both DFT + DMFT and DFT + U calculations to study the correlated electronic structure beyond DFT treating the realistic oxygen vacancy structure [Figs. 4(b)–4(e)]. DFT + U was performed with the G-type AFM ordering (the lowest-energy magnetic structure; see Table III) and DFT + DMFT was performed with the paramagnetic spin symmetry. In this structure, the six-coordinated Ni-O octahedron (Ni$_o$) and the four-coordinated Ni-O square-plane (Ni$_{sp}$) are alternating in the x-y plane as two apical oxygen ions are removed from the half of octahedra in LaNiO$_3$ [see Fig. 4(a)]. Our structural relaxation calculation shows that the Ni-O octahedron is distorted as the in-plane Ni-O bond length is larger than the out-of-plane bond (see Table II). However, the orbital energy difference between two e_g orbitals is only 0.04 eV, which is much smaller than e_g-t_{2g} splitting of 0.62 eV. In Ni$_{sp}$, the energy splitting between d_{z^2} and $d_{x^2-y^2}$ is as large as 0.8 eV.

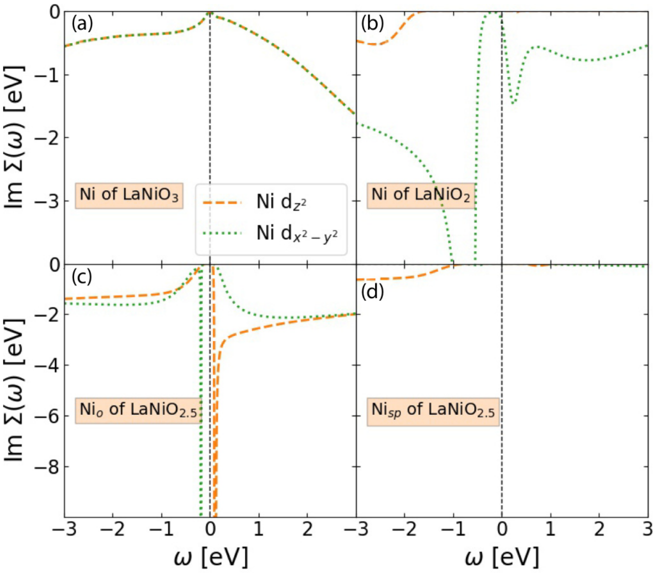

FIG. 5. Imaginary part of self-energies Im$\Sigma(\omega)$ computed for Ni d_{z^2} and $d_{x^2-y^2}$ orbitals in (a) LaNiO$_3$, (b) LaNiO$_2$, and LaNiO$_{2.5}$ for two nonequivalent Ni ions, (c) Ni$_o$ and (d) Ni$_{sp}$, respectively.

As shown in Figs. 4(b)–4(e), both DFT + DMFT and DFT + U predict the LaNiO$_{2.5}$ to be insulating consistently with experiments. This is in sharp contrast with the DFT DOS predicting the ground state to be metallic as DFT underestimates correlations (see Supplemental Material [49]). DFT + DMFT DOS opens a spectral gap of 0.3 eV resulting in the PM insulating state while the band gap computed in DFT + U with AFM becomes much larger (∼1.5 eV). Our DFT + DMFT calculation can also reveal that the two-peak structure of the unoccupied spectra measured in experiment originates from the two nonequivalent Ni ions in LaNiO$_{2.5}$. The Ni$_o$ ion [Fig. 4(b)] develops a spectral Mott gap in the middle of the almost degenerate e_g orbitals and the broad unoccupied peak near 2 eV above the Fermi energy emerges as the upper Hubbard band due to the localized nature of Ni$_o$ e_g orbitals induced by the oxygen vacancy. In Ni$_{sp}$, the d_{z^2} orbital spectra become occupied while the unoccupied DOS near 1 eV is mostly contributed from the $d_{x^2-y^2}$ orbitals also hybridized with the in-plane O 2p orbitals. Although all O ions are equivalent in LaNiO$_3$, two types of nonequivalent O ions exist in LaNiO$_{2.5}$, which are circled in Fig. 4(a) denoted as O$_A$ and O$_B$. O$_A$ is the apical oxygen of the Ni$_o$ ion and O$_B$ is the in-plane oxygen located between Ni$_o$ and Ni$_{sp}$. The O 1s XAS spectra provide a relatively unperturbed probe of the unoccupied DOS since the O 1s core hole effect is negligible [59]. However, it can probe not only O 2p but also 3d states in oxide materials due to strong d-p hybridization [60]. The O$_B$ 2p unoccupied DOS is mostly distributed near 1 eV as it is strongly hybridized with the Ni$_{sp}$ $d_{x^2-y^2}$ orbitals. The O$_A$ 2p unoccupied DOS is rather weakly hybridized with the Ni$_o$ ion showing much reduced spectra, but it is broadly distributed at higher energies than the O$_B$ spectra. In DFT + U DOS [Figs. 4(d) and 4(e)], the qualitative features of DOS are similar as the DMFT DOS confirming that the unoccupied two-peak structure is originated from two nonequivalent Ni ions. However, the DFT + U peak positions are higher in energy than the experimental peak positions.

D. Site-selective Mott insulating state in $LaNiO_{2.5}$

Here, we show the imaginary part of the self-energy on the real energy axis $\mathrm{Im}\Sigma(\omega)$ of Ni e_g orbitals computed using DMFT in Fig. 5. Two types of Ni ions in $LaNiO_{2.5}$ are plotted in Figs. 5(c) and 5(d). $LaNiO_3$ [Fig. 5(a)] and $LaNiO_2$ [Fig. 5(b)] are also compared. The self-energies of e_g orbitals in $LaNiO_3$ are degenerate and show the Fermi-liquid behavior ($\mathrm{Im}\Sigma \sim \omega^2$) at the low frequency, consistently with the metallic state. In $LaNiO_2$, the $d_{x^2-y^2}$ orbital develops correlations as the self-energy develops a pole near the Fermi energy with the large scattering rate at $\omega = 0$. In $LaNiO_{2.5}$, both Ni_o e_g orbitals have strong correlations at the Fermi energy as self-energy curves have poles right near $\omega = 0$ while Ni_{sp} in $LaNiO_{2.5}$ exhibits a flat curve. Since Ni_o e_g orbitals in $LaNiO_{2.5}$ are also nearly half-filled [see Fig. 4(a) energy diagram], this indicates a Mott-type insulator in Ni_o while the Ni_{sp} ions with oxygen vacancies behave similarly as the band insulator as only one e_g orbital is fully filled and the other e_g orbital is almost unoccupied [see Fig. 4(a) energy diagram]. This Mott insulating behavior occurs at the half of lattice sites selectivity (in this case for Ni_o sites), therefore, it can be understood as the “site-selective” Mott transition.

This site-selective Mott insulating phase is also accompanied by the substantial Ni-O bond disproportionation of 0.22 Å between Ni_o and Ni_{sp} as obtained in the DFT + U relaxation calculation (see Table II) since the Mott insulating site is expanded to reduce the hybridization between Ni and neighboring O ions. In DFT + U, this mechanism occurs as the spin-state ordering since the Mott insulating site becomes a high-spin state while the band insulating site exhibits a low-spin state. This site-selective Mott mechanism also occurs in other correlated materials including rare-earth nickelates with smaller rare-earth ions such as $LuNiO_3$ [6], the spin-state ordered $LaCoO_3$ [61], Fe_2O_3 under the high pressure [62,63], and doped manganese oxides [64]. Like the $LaNiO_3$ case with oxygen vacancies, the site-selective Mott insulating phase in other materials also accompanies some degrees of breathing-type lattice distortions as the Mott insulating site develops in an expanded octahedron and the band insulating site forms in a contracted octahedron due to strong hybridization of transition metal spins with surrounding O holes.

In DMFT calculation, one can also measure the correlation strength from the obtained quasiparticle residue Z defined as

$$Z = \left(1 - \frac{\partial\Sigma}{\partial\omega}\bigg|_{\omega=0}\right)^{-1} \tag{3}$$

which gives the inverse of the effective mass renormalization factor ($m^*/m = Z^{-1}$). The Ni e_g band of $LaNiO_3$ has an effective mass factor of 1.7. For $LaNiO_2$, electronic correlation is further enhanced than $LaNiO_3$ and the quasiparticle band of the $d_{x^2-y^2}$ orbital is strongly renormalized with a factor of 9.4. As $LaNiO_{2.5}$ with oxygen vacancies becomes an insulator, the concept of the quasiparticle mass renormalization cannot be applied any more since quasiparticles do not exist in an insulator.

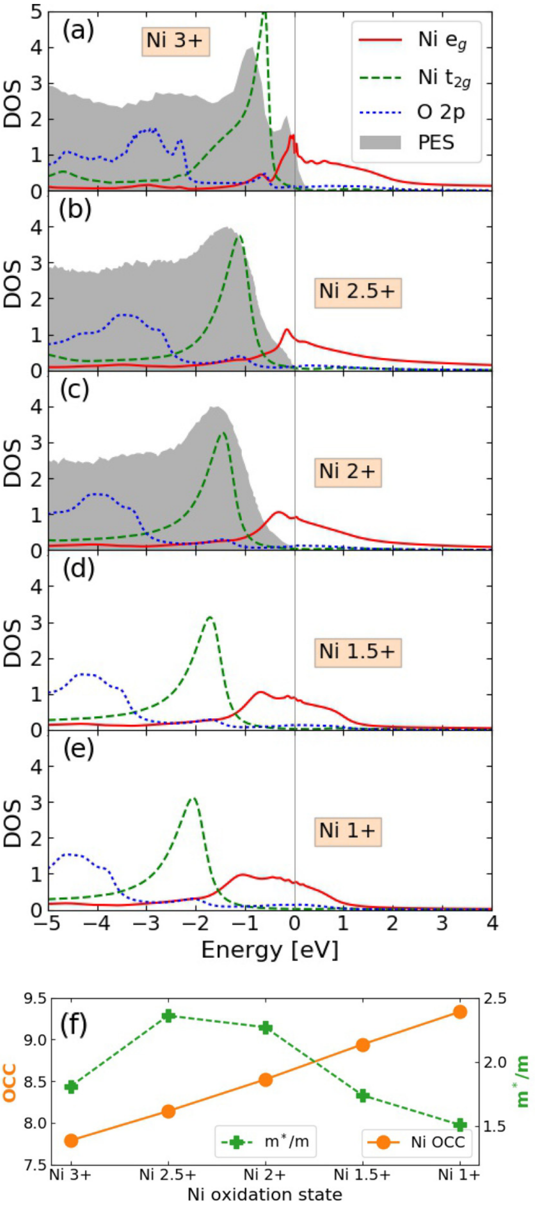

FIG. 6. (a)–(e) DFT + DMFT DOS of $LaNiO_{3-x}$ systems at different Ni oxidation states computed using the rigid band-shift approximation. (f) The d occupancy and the mass renormalization factor as a function of different Ni oxidation states.

Oxygen vacancy also changes the Ni oxidation state and increases the electron occupation in the Ni-O manifold effectively as two electrons are donated from the removed oxygen ion. Table V shows the occupation number for Ni 3d and O 2p orbitals in each structure obtained from DFT + DMFT and DFT + U. In DFT + DMFT calculations, as the Ni oxidation state changes from Ni^{3+} in $LaNiO_3$ to Ni^{1+} in $LaNiO_2$, the d-orbital occupancy increases from 7.8 to 9.12 and the hole occupancy in the O ion decreases from 0.26 to 0.06. DFT + U also shows the increase of the average d-orbital occupancy from $LaNiO_3$ to $LaNiO_2$, however, its value is larger than the DFT + DMFT result. In $LaNiO_{2.5}$, the average Ni oxidation state is Ni^{2+}. However, it is not clear whether the electron transfer due to oxygen vacancy will occur mostly to Ni_{sp} resulting in charge ordering between Ni^{3+} in the Ni_o ion and Ni^{1+} in the Ni_{sp} ion or both Ni_o and Ni_{sp} ions will have the similar Ni^{2+} configuration without charge ordering. Our DFT + DMFT calculation shows that Ni_o is close to Ni^{2+} as the e_g orbitals in Ni_o are almost half-filled ($\sim$2.13) and the e_g occupancy in Ni_{sp} is slightly more occupied than the half-filling leaving some holes per the O site ($\sim$0.15). This hole state in O is rather strongly hybridized with the Ni_{sp} e_g orbital as shown in the previous DOS result. Therefore, the site-selective Mott transition in $\mathrm{LaNiO}_{2.5}$ also leads to small charge ordering between Ni_o and Ni_{sp} ions. DFT + U also shows the similar charge ordering in $\mathrm{LaNiO}_{2.5}$.

E. Rigid band-shift approximation in LaNiO_{3-x}

Our DFT + DMFT calculation in $\mathrm{LaNiO}_{2.5}$ shows that the paramagnetic insulating phase in $\mathrm{LaNiO}_{2.5}$ originates from the change of Ni oxidation states as well as the oxygen vacancy-ordering structure which induces both the local symmetry change of Ni ions and different hybridization of Ni ions with surrounding O ions. To investigate the effect of the oxygen vacancy-ordering structure on electronic correlations, we apply the rigid band-shift approximation to LaNiO_3 within DFT + DMFT to impose the effect of the Ni oxidation state change alone. In this approximation, we use the same Wannier band structure obtained from LaNiO_3 at different vacancy levels while the effect of different Ni oxidation states is adopted by shifting the Fermi level to modify the total number of electrons within DMFT calculations accordingly.

Figures 6(a)–6(e) show the DOS of different Ni oxidation states due to the change of vacancy level x, namely, Ni^{3+} for $x = 0$ and Ni^{1+} for $x = 1$. As the oxidation number changes from Ni^{3+} to Ni^{1+}, O p and Ni t_{2g} states move further below the Fermi energy while keep the shape mostly unchanged. This trend is also consistent with the experiment data depicted as the shaded region. The Ni e_g states near the Fermi energy also do not change significantly as the Fermi level shifts higher in energy for the smaller oxidation state. The Ni^{2+} state corresponding to $\mathrm{LaNiO}_{2.5}$ still exhibits the metallic state without developing a Mott state although the e_g occupancy becomes close to the half-filling. In Fig. 6(f), we plot the mass renormalization factor m^*/m and the corresponding Ni d occupancies as a function of Ni oxidation states. While the d occupancies change linearly, the effective mass becomes maximum only when the d occupancy becomes close to 8.0, meaning the half-filled e_g occupancy although the mass renormalization remains in range of 1.5–2.5. Therefore, the strong correlation effect occurring in the oxygen vacancy structure cannot be captured by the Ni oxidation change alone within the rigid band-shift approximation.

IV. CONCLUSION

In conclusion, we performed first-principles calculations in LaNiO_3 with oxygen vacancies (LaNiO_{3-x} with $x = 0$, 0.25, 0.5, 0.75, and 1). Experimentally, the metal-to-insulator transition occurs as the oxygen vacancy level x approaches to 0.5 and the ground state is AFM (AFM becomes PM at higher temperature). We find that the vacancy ordering structure of alternating NiO_6 octahedra and NiO_4 square planes (with apical oxygen vacancies) becomes thermodynamically stable in $\mathrm{LaNiO}_{2.5}$ when the oxygen pressure is lowered than the typical growth condition of LaNiO_3. DFT + U converges to the correct AFM magnetic order in $\mathrm{LaNiO}_{2.5}$ while DFT favors FM implying that the electronic correlation effect can be important for oxygen vacancy structures. Our DFT + DMFT calculation in $\mathrm{LaNiO}_{2.5}$ shows that the PM state is insulating and the nature of this insulating state is the site-selective Mott phase in which the octahedral Ni ion develops a Mott state with strong electron correlations and the square-planar Ni ion becomes a band insulator with the negligible self-energy. We also explain the nature of the two-peak structure in unoccupied spectra measured in O 1s XAS experiments of LaNiO_{3-x}. The lower-energy peak in XAS originates from the square-planar Ni state strongly hybridized with O ions while the higher-energy peak is resulted from the broad spectra of the localized e_g orbitals in strongly correlated octahedral Ni ion. LaNiO_2 with the complete apical oxygen vacancies becomes also strongly correlated as it reduces the Ni-O hybridization and lifts the degeneracy between e_g orbitals, as a result, it becomes close to the Mott state although it is still metallic.

The change of Ni oxidation states alone within the rigid band-shift approximation cannot capture the strongly correlated insulating phase occurring in the oxygen vacancy structure of LaNiO_3 implying that it is important to treat realistic oxygen vacancy structures of materials using first principles to account for electronic correlation effects induced by oxygen vacancies. Moreover, the Hubbard U values of Ni ions can be site dependent in oxygen vacancy structures since chemical environments of Ni ions can be varied due to oxygen vacancies. In principle, site-dependent U values can be computed from first principles, and their effects on electronic structure of materials with oxygen vacancies can be an interesting topic for future studies.

ACKNOWLEDGMENTS

X.L. and H.P. are supported by the Materials Sciences and Engineering Division, Basic Energy Sciences, Office of Science, U.S. DOE. The part of this work related to the vacancy formation energy calculation is supported by ACS-PRF Grant No. 60617. V.S. is supported by the NSF SI2-SSE Grant No. 1740112. We gratefully acknowledge the computing resources provided on Bebop, a high-performance computing cluster operated by the Laboratory Computing Resource Center at Argonne National Laboratory.

---

[1] G. Catalan, Phase Trans. **81**, 729 (2008).
[2] P. Zubko, S. Gariglio, M. Gabay, P. Ghosez, and J.-M. Triscone, Annu. Rev. Condens. Matter Phys. **2**, 141 (2011).

[3] J. A. Alonso, M. J. Martínez-Lope, M. T. Casais, J. L. García-Muñoz, and M. T. Fernández-Díaz, Phys. Rev. B **61**, 1756 (2000).

[4] U. Staub, G. I. Meijer, F. Fauth, R. Allenspach, J. G. Bednorz, J. Karpinski, S. M. Kazakov, L. Paolasini, and F. d'Acapito, Phys. Rev. Lett. **88**, 126402 (2002).

[5] J.-S. Zhou, J. B. Goodenough, B. Dabrowski, P. W. Klamut, and Z. Bukowski, Phys. Rev. Lett. **84**, 526 (2000).

[6] H. Park, A. J. Millis, and C. A. Marianetti, Phys. Rev. Lett. **109**, 156402 (2012).

[7] S. Catalano, M. Gibert, J. Fowlie, J. Íñiguez, J.-M. Triscone, and J. Kreisel, Rep. Prog. Phys. **81**, 046501 (2018).

[8] F. Gunkel, D. V. Christensen, Y. Z. Chen, and N. Pryds, Appl. Phys. Lett. **116**, 120505 (2020).

[9] R. Eguchi, A. Chainani, M. Taguchi, M. Matsunami, Y. Ishida, K. Horiba, Y. Senba, H. Ohashi, and S. Shin, Phys. Rev. B **79**, 115122 (2009).

[10] M. K. Stewart, C.-H. Yee, J. Liu, M. Kareev, R. K. Smith, B. C. Chapler, M. Varela, P. J. Ryan, K. Haule, J. Chakhalian, and D. N. Basov, Phys. Rev. B **83**, 075125 (2011).

[11] D. G. Ouellette, S. B. Lee, J. Son, S. Stemmer, L. Balents, A. J. Millis, and S. J. Allen, Phys. Rev. B **82**, 165112 (2010).

[12] T. Moriga, O. Usaka, I. Nakabayashi, T. Kinouchi, S. Kikkawa, and F. Kanamaru, Solid State Ionics **79**, 252 (1995), Proceedings of the 20th Commemorative Symposium on Solid State Ionics in Japan.

[13] R. D. Sánchez, M. T. Causa, A. Caneiro, A. Butera, M. Vallet-Regí, M. J. Sayagués, J. González-Calbet, F. García-Sanz, and J. Rivas, Phys. Rev. B **54**, 16574 (1996).

[14] D. Kaneko, K. Yamagishi, A. Tsukada, T. Manabe, and M. Naito, Physica C (Amsterdam) **469**, 936 (2009), Proceedings of the 21st International Symposium on Superconductivity (ISS 2008).

[15] D. Li, K. Lee, B. Wang, M. Osada, S. Crossley, H. R. Lee, Y. Cui, Y. Hikita, and H. Y. Hwang, Nature (London) **572**, 624 (2019).

[16] M. Osada, B. Y. Wang, B. H. Goodge, K. Lee, H. Yoon, K. Sakuma, D. Li, M. Miura, L. F. Kourkoutis, and H. Y. Hwang, Nano Lett. **20**, 5735 (2020).

[17] H. Guo, Z. W. Li, L. Zhao, Z. Hu, C. F. Chang, C.-Y. Kuo, W. Schmidt, A. Piovano, T. W. Pi, O. Sobolev, D. I. Khomskii, L. H. Tjeng, and A. C. Komarek, Nat. Commun. **9**, 43 (2018).

[18] J. Zhang, H. Zheng, Y. Ren, and J. F. Mitchell, Cryst. Growth Des. **17**, 2730 (2017).

[19] B.-X. Wang, S. Rosenkranz, X. Rui, J. Zhang, F. Ye, H. Zheng, R. F. Klie, J. F. Mitchell, and D. Phelan, Phys. Rev. Materials **2**, 064404 (2018).

[20] M. A. Hayward, M. A. Green, M. J. Rosseinsky, and J. Sloan, J. Am. Chem. Soc. **121**, 8843 (1999).

[21] M. Abbate, G. Zampieri, F. Prado, A. Caneiro, J. M. Gonzalez-Calbet, and M. Vallet-Regi, Phys. Rev. B **65**, 155101 (2002).

[22] K. Horiba, R. Eguchi, M. Taguchi, A. Chainani, A. Kikkawa, Y. Senba, H. Ohashi, and S. Shin, Phys. Rev. B **76**, 155104 (2007).

[23] M. Golalikhani, Q. Lei, R. U. Chandrasena, L. Kasaei, H. Park, J. Bai, P. Orgiani, J. Ciston, G. E. Sterbinsky, D. A. Arena, P. Shafer, E. Arenholz, B. A. Davidson, A. J. Millis, A. X. Gray, and X. X. Xi, Nat. Commun. **9**, 2206 (2018).

[24] D. Misra and T. K. Kundu, Eur. Phys. J. B **89**, 4 (2016).

[25] A. Malashevich and S. Ismail-Beigi, Phys. Rev. B **92**, 144102 (2015).

[26] M. Kotiuga, Z. Zhang, J. Li, F. Rodolakis, H. Zhou, R. Sutarto, F. He, Q. Wang, Y. Sun, Y. Wang, N. A. Aghamiri, S. B. Hancock, L. P. Rokhinson, D. P. Landau, Y. Abate, J. W. Freeland, R. Comin, S. Ramanathan, and K. M. Rabe, Proc. Natl. Acad. Sci. USA **116**, 21992 (2019).

[27] A. Subedi, SciPost Phys. **5**, 20 (2018).

[28] S. Bandyopadhyay, P. Adhikary, T. Das, I. Dasgupta, and T. Saha-Dasgupta, Phys. Rev. B **102**, 220502(R) (2020).

[29] A. S. Botana and M. R. Norman, Phys. Rev. X **10**, 011024 (2020).

[30] J. Karp, A. S. Botana, M. R. Norman, H. Park, M. Zingl, and A. Millis, Phys. Rev. X **10**, 021061 (2020).

[31] S. Ryee, H. Yoon, T. J. Kim, M. Y. Jeong, and M. J. Han, Phys. Rev. B **101**, 064513 (2020).

[32] P. Werner and S. Hoshino, Phys. Rev. B **101**, 041104(R) (2020).

[33] F. Lechermann, Phys. Rev. B **101**, 081110(R) (2020).

[34] Y. Wang, C.-J. Kang, H. Miao, and G. Kotliar, Phys. Rev. B **102**, 161118(R) (2020).

[35] G. Kresse and J. Furthmüller, Phys. Rev. B **54**, 11169 (1996).

[36] G. Kresse and D. Joubert, Phys. Rev. B **59**, 1758 (1999).

[37] J. P. Perdew, A. Ruzsinszky, G. I. Csonka, O. A. Vydrov, G. E. Scuseria, L. A. Constantin, X. Zhou, and K. Burke, Phys. Rev. Lett. **100**, 136406 (2008).

[38] V. Singh, U. Herath, B. Wah, X. Liao, A. H. Romero, and H. Park, Comput. Phys. Commun. **261**, 107778 (2021).

[39] N. Marzari and D. Vanderbilt, Phys. Rev. B **56**, 12847 (1997).

[40] I. Souza, N. Marzari, and D. Vanderbilt, Phys. Rev. B **65**, 035109 (2001).

[41] J. Ruppen, J. Teyssier, O. E. Peil, S. Catalano, M. Gibert, J. Mravlje, J.-M. Triscone, A. Georges, and D. van der Marel, Phys. Rev. B **92**, 155145 (2015).

[42] A. Hampel, P. Liu, C. Franchini, and C. Ederer, npj Quantum Mater. **4**, 5 (2019).

[43] H. Park, A. J. Millis, and C. A. Marianetti, Phys. Rev. B **89**, 245133 (2014).

[44] E. A. Nowadnick, J. P. Ruf, H. Park, P. D. C. King, D. G. Schlom, K. M. Shen, and A. J. Millis, Phys. Rev. B **92**, 245109 (2015).

[45] G. Gou, I. Grinberg, A. M. Rappe, and J. M. Rondinelli, Phys. Rev. B **84**, 144101 (2011).

[46] H. Park, A. J. Millis, and C. A. Marianetti, Phys. Rev. B **90**, 235103 (2014).

[47] E. Gull, A. J. Millis, A. I. Lichtenstein, A. N. Rubtsov, M. Troyer, and P. Werner, Rev. Mod. Phys. **83**, 349 (2011).

[48] K. Haule, Phys. Rev. B **75**, 155113 (2007).

[49] See Supplemental Material at http://link.aps.org/supplemental/10.1103/PhysRevB.103.085110 for DFT/DFT + U electronic structures and total energies of LNO systems and calculation method details.

[50] A. Wold, B. Post, and E. Banks, J. Am. Chem. Soc. **79**, 4911 (1957).

[51] J. A. Alonso, M. J. Martínez-Lope, J. L. García-Muñoz, and M. T. Fernández-Díaz, J. Phys.: Condens. Matter **9**, 6417 (1997).

[52] T. Moriga, O. Usaka, T. Imamura, I. Nakabayashi, I. Matsubara, T. Kinouchi, K. Shinichi, and F. Kanamaru, Bull. Chem. Soc. Jpn. **67**, 687 (1994).

[53] J. L. García-Muñoz, J. Rodríguez-Carvajal, P. Lacorre, and J. B. Torrance, Phys. Rev. B **46**, 4414 (1992).

[54] B. Geisler and R. Pentcheva, Phys. Rev. B **101**, 165108 (2020).
[55] K. Reuter and M. Scheffler, Phys. Rev. B **65**, 035406 (2001).
[56] R. Pentcheva, F. Wendler, H. L. Meyerheim, W. Moritz, N. Jedrecy, and M. Scheffler, Phys. Rev. Lett. **94**, 126101 (2005).
[57] N. Mulakaluri, R. Pentcheva, M. Wieland, W. Moritz, and M. Scheffler, Phys. Rev. Lett. **103**, 176102 (2009).
[58] M. Hepting, D. Li, C. J. Jia, H. Lu, E. Paris, Y. Tseng, X. Feng, M. Osada, E. Been, Y. Hikita, Y.-D. Chuang, Z. Hussain, K. J. Zhou, A. Nag, M. Garcia-Fernandez, M. Rossi, H. Y. Huang, D. J. Huang, Z. X. Shen, T. Schmitt *et al.*, Nat. Mater. **19**, 381 (2020).
[59] E. Z. Kurmaev, R. G. Wilks, A. Moewes, L. D. Finkelstein, S. N. Shamin, and J. Kuneš, Phys. Rev. B **77**, 165127 (2008).
[60] I. Timrov, P. Agrawal, X. Zhang, S. Erat, R. Liu, A. Braun, M. Cococcioni, M. Calandra, N. Marzari, and D. Passerone, Phys. Rev. Research **2**, 033265 (2020).
[61] H. Park, R. Nanguneri, and A. T. Ngo, Phys. Rev. B **101**, 195125 (2020).
[62] E. Greenberg, I. Leonov, S. Layek, Z. Konopkova, M. P. Pasternak, L. Dubrovinsky, R. Jeanloz, I. A. Abrikosov, and G. K. Rozenberg, Phys. Rev. X **8**, 031059 (2018).
[63] I. Leonov, G. K. Rozenberg, and I. A. Abrikosov, npj Comput. Mater. **5**, 90 (2019).
[64] A. Valli, H. Das, G. Sangiovanni, T. Saha-Dasgupta, and K. Held, Phys. Rev. B **92**, 115143 (2015).